Heat and Mass Transfer
https://doi.org/10.1007/s00231-022-03329-5

ORIGINAL

On an averaged energy-balance method for the analysis of wavy microchannels

Roxana Durantes[1] · Justin Moon[1] · J. Rafael Pacheco[2] · Arturo Pacheco-Vega[1]

Received: 16 March 2022 / Accepted: 28 November 2022

Abstract

This study presents numerical simulations of the convective heat transfer on wavy microchannels to investigate heat transfer enhancement in these systems. The objective is to propose a methodology based on local and global energy balances in the device, instead of the commonly used Nusselt number, as an alternative for the thermal analysis. This investigation is carried out on a single-wave microchannel model of size 0.5 mm by 0.5 mm by 20 mm length, with water flowing inside the channel, exposed to a heat influx of 47 W/cm^2 at the bottom. The governing equations for an incompressible laminar flow and conjugate heat transfer are first built, and then solved, for representative models, with copper as the solid-block material under a number of operating conditions (cold-water flowrates of $Re = 50$, 100, and 150), by the finite element technique. From computed velocity, pressure and temperature fields, local and global energy balances based on cross-section-averaged velocities and temperatures enable calculating the heat rate at each section of the corresponding device. Results from this study for two different designs, namely, serpentine and divergent-convergent layouts, show that this so-called averaged energy-balance methodology enables higher accuracy than that based on Nusselt numbers since neither transfer coefficients nor characteristic temperatures are needed.

Keywords Microchannels · Wavy configuration · Heat transfer enhancement · Conjugate heat transfer · Forced convection

Abbreviations

A	wave amplitude
A_{base}	base area for heat influx
A_w	heat transfer surface area
c_p	specific heat
D_h	hydraulic diameter
k	thermal conductivity
ΔL	length of subsection
N	number of subsections
n	outward-direction coordinate
$\mathbf{n}$	outward unit vector
p	pressure
Δp	pressure drop
q''	heat flux
Q	heat transfer rate
Q_{in}	input heat rate
Re	Reynolds number
T	temperature of fluid
T_s	temperature of solid
$\mathbf{u}$	Cartesian velocity vector
u, v, w	Cartesian velocities
u_{in}	inlet frontal velocity
x^*	local streamwise coordinate
x, y, z	Cartesian coordinates

Greek symbols

λ	wavelength
μ	dynamic viscosity
ν	kinematic viscosity
ρ_f	density of fluid
ρ_s	density of solid
Ω_f	fluid domain
Ω_s	solid domain
ϕ	phase angle

Subscripts and superscripts

$\overline{(\cdot)}$	cross-sectional-averaged values
f	fluid
in	inlet
j	j-th channel subsection
out	outlet
s	solid

✉ Arturo Pacheco-Vega
apacheco@calstatela.edu

[1] Department of Mechanical Engineering, California State University - Los Angeles, Los Angeles, CA 90032, USA

[2] SAP America Inc, Tempe 85281, USA

Published online: 07 January 2023

1 Introduction

The continuous advancement in miniaturization and scaling of integrated circuits, for high power-density electronic applications, has increased the demand for devices with improved heat removal capabilities. In these applications, intervention in the form of thermal management is key to prolong working life and increase reliability of electronic devices where significant amounts of heat are generated. Although many alternatives have been proposed to solve this problem, an approach based on microchannels was suggested by Tuckerman and Pease [1], several years ago. Since then, a number of studies and reviews has been conducted [2–5], including experimental and numerical analyses of microchannel devices using single-phase fluids [6–10].

In recent years, several exploratory studies of microchannel designs have revealed the possibility of enhancing the transfer of energy in electronic equipment with a reasonable pressure drop. A specific case is that of the wavy geometry (as compared to a straight channel), which is designed to enhance heat transfer by improving fluid mixing and enlarging surface area. For this type of configuration, several works have confirmed that although slightly larger pressure drop along the channel occurs, there is a substantial increase in heat transfer [11–13]. For some geometries and small fluid velocities, however, some deterioration of the thermal performance was also observed and reported, with attempts to address this problem being made by a number of investigations based on the single-wavelength wavy channel configuration [14–16].

Further development of microchannel designs have also included studies related to the influence of geometry selection [17, 18], or the conductive materials enclosing the fluid-flow channel [19], upon the enhancement of heat transfer. For instance, with focus on the effect of channel surface topography on the enhancing mechanisms in wavy microchannels, recent work by Moon et al. [17] has shown that the addition of harmonic surfaces to the basic wavy topology provides higher Nusselt number ratios. On the other hand, by considering a variety of conductive materials; e.g., aluminum and silicon, in addition to the typical copper, for the solid block that encloses the channel, Moon et al. [19] showed that, regardless of the material, as wave amplitude and Reynolds number increase, and so does the effectiveness of the device, and though the selection of specific material highly influences the diffusion of heat in the solid, it is negligible on the Nusselt number for the fluid. Moreover, these works also found a decrease in the efficiency of the system, which was concluded to be due to the coupling of the pressure drop and the specific Nusselt number definition in the so-called performance factor (also known as performance evaluation criterion). It is important to note that a common thread among all the aforementioned studies is the use of the Nusselt number as basis for the analysis. Nusselt numbers enable generality in the analysis since different fluids and temperatures can be used. However, as pointed out by Pacheco-Vega et al. [20, 21], if accuracy is the goal, it may be better to compute the heat rate directly since uncertainties – due to assumptions like the existence of a heat transfer coefficient, or a unique characteristic temperature difference for the system, particularly for those systems with high level of complexity – are significantly reduced. This is what we propose to do within the context of microchannels.

In the present study we expand our previous work on the conjugate heat transfer characteristics of wavy microchannels [17, 19], by considering a methodology that uses the heat transfer rate instead of the common Nusselt number as the basis for the calculations. In the context of compact heat exchangers, this approach has been shown to provide higher accuracy at the expense of less generality [22–26]. To this end, we restrict ourselves to single-wave microchannel models and build for them the corresponding conjugate heat transfer equations. Later, the model equations are solved on a representative computational domain using the finite element method, to obtain velocity-, pressure- and temperature-fields for the fluid in the microchannel, and the temperature distribution in the corresponding solid block. Finally, values of the pressure drop, inlet-to-outlet fluid and the heat rate (computed from local and global energy balances), are used to assess the relative system performance for the two types of microchannel geometries considered.

2 Problem description and mathematical model

The microchannel device – illustrated schematically in Fig. 1 – has a single-wave wall profile of a typical cooling system of a circuit-energy-dissipating equipment. The model (namely the baseline for our calculations), consists of a square cross-section channel that is enclosed by a copper block. The dimensions of the channel are: 500 μm × 500 μm × 20 mm, with two 2 mm inlet- and outlet-straight sections and a 16 mm middle wavy section, as shown in Fig. 1. The block has a shape of a square duct of thickness 1.5 mm and length 20 mm. A heat flux of 47 W/cm^2 is uniformly applied at the bottom surface and it is advected out of the system through the internal flow of water in the channel. The set of microchannel-block designs herein studied, referred to as *wavy* configuration, has sinusoidal profiles at both the top and the bottom surfaces, based on the function

$$y(x^*) = A \sin\left(\frac{2\pi x^*}{\lambda} + \phi\right), \tag{1}$$

where $x^* = x - 2$ is a local streamwise coordiante in $x^* \in [0, 16]$ mm (as defined in Fig. 1), and x and y refer to the streamwise and vertical directions, respectively, for $z \in [-250, 250]$ μm, A as the wave amplitude and λ is its wavelength. The angle ϕ in the equation is used to distinguish between the two different types of wavy channel configurations analyzed. For instance, the first type, shown in Fig. 1a, corresponds to a serpentine layout in which the crests and troughs of the top- and bottom-walls are aligned. For this arrangement, both walls are set up with $\phi = 0$ in Eq. (1). On the other hand, the second type, illustrated in Fig. 1b, corresponds to a divergent-convergent design in which the crests and troughs of the top- and bottom-walls are opposed. For this layout, $\phi = 0$ in Eq. (1) is used for the top wall while $\phi = \pi$ (= 180°) is used for the bottom wall.

The governing equations correspond to a three-dimensional conjugate model for two domains: the channel inside of which water flows Ω_f, and the solid block Ω_s surrounding it. For Ω_f, we consider the incompressible flow of a Newtonian fluid, with constant properties, in the laminar regime, under steady-state conditions, without body forces and viscous dissipation, and a negligible radiative heat transfer. Thus, the mathematical model is given in expanded form as

$$\frac{\partial u}{\partial x} + \frac{\partial v}{\partial y} + \frac{\partial w}{\partial z} = 0, \tag{2}$$

$$u\frac{\partial u}{\partial x} + v\frac{\partial u}{\partial y} + w\frac{\partial u}{\partial z} = -\frac{1}{\rho_f}\frac{\partial p}{\partial x} + \nu_f\left(\frac{\partial^2 u}{\partial x^2} + \frac{\partial^2 u}{\partial y^2} + \frac{\partial^2 u}{\partial z^2}\right), \tag{3}$$

$$u\frac{\partial v}{\partial x} + v\frac{\partial v}{\partial y} + w\frac{\partial v}{\partial z} = -\frac{1}{\rho_f}\frac{\partial p}{\partial y} + \nu_f\left(\frac{\partial^2 v}{\partial x^2} + \frac{\partial^2 v}{\partial y^2} + \frac{\partial^2 v}{\partial z^2}\right), \tag{4}$$

$$u\frac{\partial w}{\partial x} + v\frac{\partial w}{\partial y} + w\frac{\partial w}{\partial z} = -\frac{1}{\rho_f}\frac{\partial p}{\partial z} + \nu_f\left(\frac{\partial^2 w}{\partial x^2} + \frac{\partial^2 w}{\partial y^2} + \frac{\partial^2 w}{\partial z^2}\right), \tag{5}$$

$$u\frac{\partial T}{\partial x} + v\frac{\partial T}{\partial y} + w\frac{\partial T}{\partial z} = \frac{k_f}{\rho_f c_{p,f}}\left(\frac{\partial^2 T}{\partial x^2} + \frac{\partial^2 T}{\partial y^2} + \frac{\partial^2 T}{\partial z^2}\right). \tag{6}$$

For Ω_s, on the other hand, the energy equation for a homogeneous solid material is given by

$$\frac{k_s}{\rho_s c_{p,s}}\left(\frac{\partial^2 T_s}{\partial x^2} + \frac{\partial^2 T_s}{\partial y^2} + \frac{\partial^2 T_s}{\partial z^2}\right) = 0. \tag{7}$$

In Eqs. (2)-(6), u, v and w, are the velocity components in the x-, y-, and z-direction, respectively; p is the fluid pressure, ρ_f is its density, and $c_{p,f}$ is the specific heat, k_f the fluid thermal conductivity, $\nu_f = \mu_f/\rho_f$ is the kinematic viscosity and T its temperature. For the solid block, k_s, ρ_s, $c_{p,s}$ and T_s, in Eq. (7), are the thermal conductivity, density and specific heat of the block material, and its corresponding temperature, respectively. Tables 1 and 2 show the values of properties for both fluid (water) and solid (copper), that are used in this study, at a reference temperature of 300 K. It is important to note that, though the use of variable properties in the governing equations could slightly improve the accuracy in the calculations, once the numerical data have been computed, their use will not qualitatively change the outcomes from the analysis (whether using Nusselt numbers or the present approach). Justification on the use of constant properties for these calculations has been widely reported in the scientific literature; e.g. [27, 28], among several others.

Table 1 Fluid properties used in simulations

Parameter	*Description*	*Value*
k_f	Thermal conductivity	0.61 W/m · K
$c_{p,f}$	Specific heat	4.182 kJ/kg · K
ρ_f	Fluid density	908.4 kg/m^3
μ_f	Dynamic viscosity	1.007×10^{-3} Pa · s

The boundary conditions are as follows. For the channel domain Ω_f: (1) a prescribed streamwise velocity $u = u_{in}$ at the inlet of the channel, (2) zero-pressure and zero-viscous stresses at the outlet, (3) no-slip and no-penetration conditions are imposed at the channel walls. In addition, (4) at the inlet, we prescribe a uniform temperature of $T_{in} = 300$ K; (5) at the solid-fluid interface walls we impose conditions of continuity of both temperature; i.e., $T = T_s$, and heat flux; i.e., $k_f \partial T/\partial n = k_s \partial T_s/\partial n$; (6) at the outlet, conditions of zero temperature gradients; i.e., $\partial T/\partial n = 0$, are also imposed. For the solid block domain, Ω_s: (7) the heat-generating chip is modeled by considering uniform heat influx of $q'' = 47$ W/cm^2, at the bottom surface (on a 10 mm × 1.5 mm area) with all other surface boundaries of the solid being considered adiabatic. Finally, for the entire system: (8) conditions of symmetry at the mid-plane, $z = 0$, are prescribed since not only they arise naturally but also enable reduction of CPU times.

Table 2 Solid properties used in simulations.

Parameter	*Description*	*Value*
k_s	Thermal conductivity	403.7 W/m · K
$c_{p,s}$	Specific heat	0.375 kJ/kg · K
ρ_s	Solid density	8933 kg/m^3

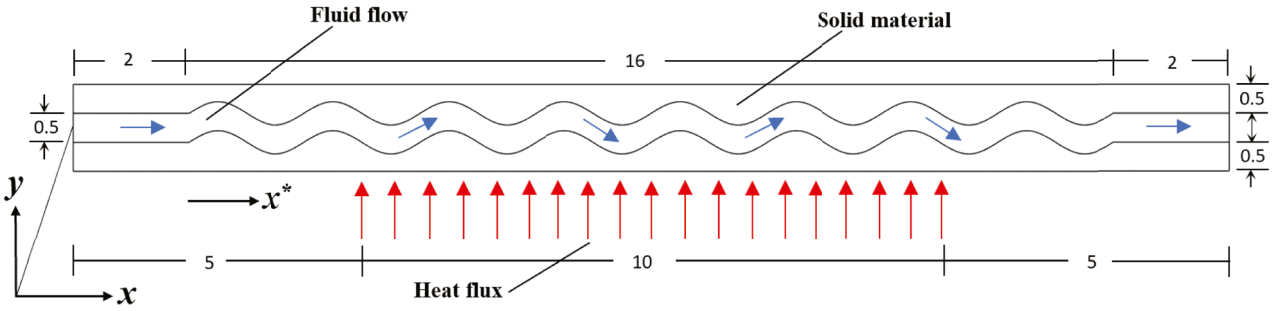

(a) In Eq. (1), top wall: $\phi = 0$; bottom wall: $\phi = 0$.

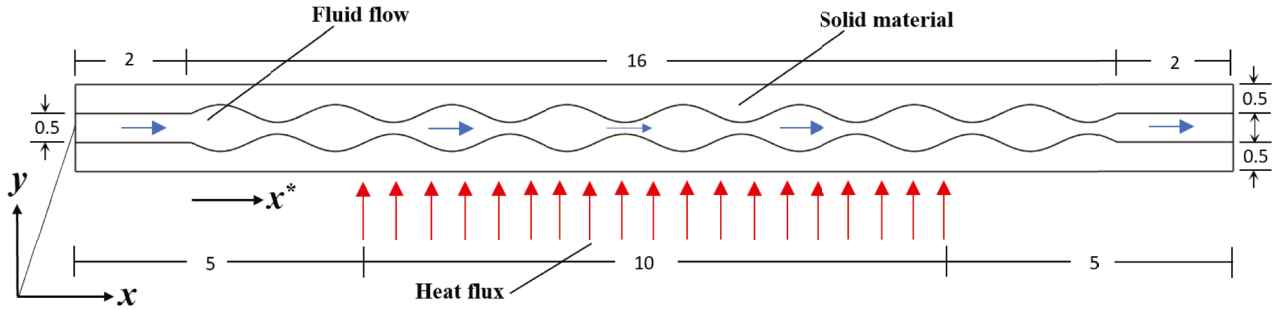

(b) In Eq. (1), top wall: $\phi = 0$; bottom wall: $\phi = \pi$.

Fig. 1 Schematic side view of a wavy microchannel geometry (dimensions in mm)

3 Solution method and grid independence

The governing Eqs. (2)-(7), were first discretized on the channel Ω_f, and solid-block Ω_s, domains using finite elements, and then solved with the multi-purpose software COMSOL Multiphysics (http://www.comsol.com). The procedure used is as follows. For each geometry considered, we use three-dimensional unstructured meshes with four-node tetrahedral elements for fluid temperature, velocity and pressure, as well as for temperatures within the solid. Since a sharp representation of the fluid-solid interface is necessary to enable accurate solutions in regions close to the walls, a mesh comprised of hexahedral elements is applied in those regions. Figure 2 illustrates a typical meshing of both computational domains. The resulting system of algebraic equations is then solved iteratively by the Generalized Minimum Residual (GMRES) solver. The relative tolerance for calculations of velocity, pressure and temperatures in the channel, and temperatures in the solid

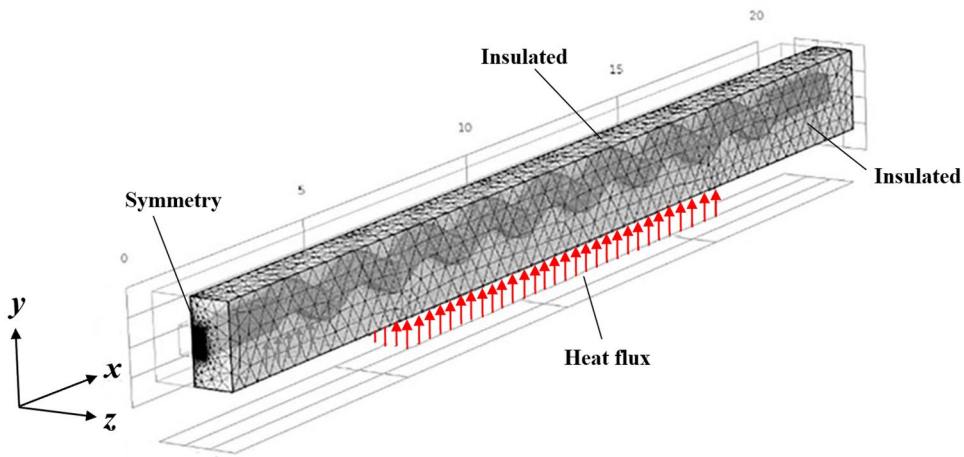

Fig. 2 Typical mesh of channel and solid block domains

block, is set to 10^{-6}. At the inlet of the channel-block system, a discontinuous Galerkin condition [29] is used to accurately setup the thermal condition for the fluid (T_{in} = constant) and the solid ($\partial T_s/\partial n = 0$) domains, and sharply distinguish between them at the fluid-solid interface. Independence of numerical results from grid size is achieved with tests of various models with different grid sizes and values of inlet velocity. A typical set of convergence tests is illustrated in Fig. 3 for the fluid pressure p, streamwise velocity u and temperature T, at a fixed point in the domain Ω_f. As indicated before, the model is that of a single wavelength configuration with a hydraulic diameter, of $D_h = 500$ μm, a wave amplitude of $A = 200$ μm and a Reynolds number, defined as $Re = D_h u_{in} \rho_f / \mu_f$, of $Re = 150$. From the figure it can be seen that the error values in u and p vary significantly in the range of [2.9,3.4] million elements – with those of T being essentially zero – but they rapidly decline as the number of elements increases (i.e., the mesh size is reduced). In fact, a mesh with 3.6 million elements is sufficient to achieve an accuracy within 0.5% of that obtained by the maximum number of elements (4.8 million). In the case of the solid-block material, a maximum number of only 282,000 elements is necessary to achieve grid independence of the solution (the error with respect to a grid with 900,000 elements, is essentially zero. Thus, in this work, a total number of 3.6 million elements are used for the domain comprising both solid and fluid regions. It is to note that typical CPU times are about 11 hours per run.

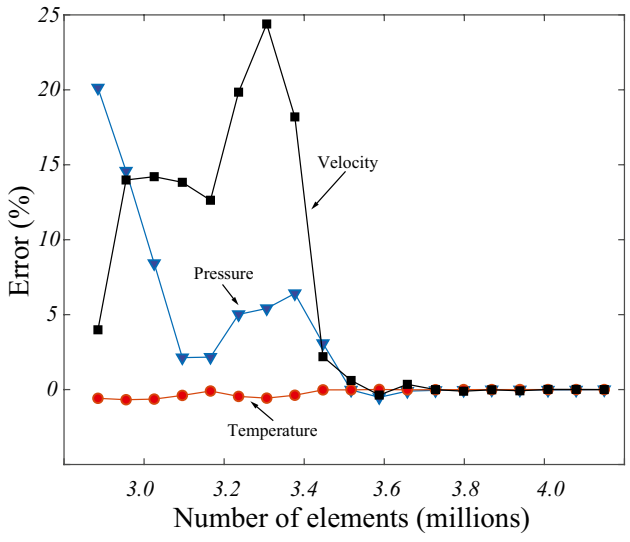

Fig. 3 Typical mesh of computational domain and grid independence tests

4 Results and analysis

4.1 Hydrodynamics and heat transfer

Solutions of the steady-state conjugate heat transfer model for the single-wave system Eqs. (2)-(7), provided in Figs. 4, 5 and 6 for the two designs, were computed for five values of wave amplitude $A = \{0, 50, 100, 150, 200\}$ μm, and three values of Reynolds number $Re = \{50, 100, 150\}$, with a wavelength of $\lambda = 2$ mm and a heat influx $q'' = 47$ W/cm^2. Figure 4, with Fig. 4a presenting those for the serpentine layout and Fig. 4b those for the divergent-convergent arrangement, shows a comparison of the results for the pressure drop Δp, as a function of A and Re, to those of Gong et al. [13]. From the figure it can be observed that our numerical solutions not only qualitatively follow the same trend as those of

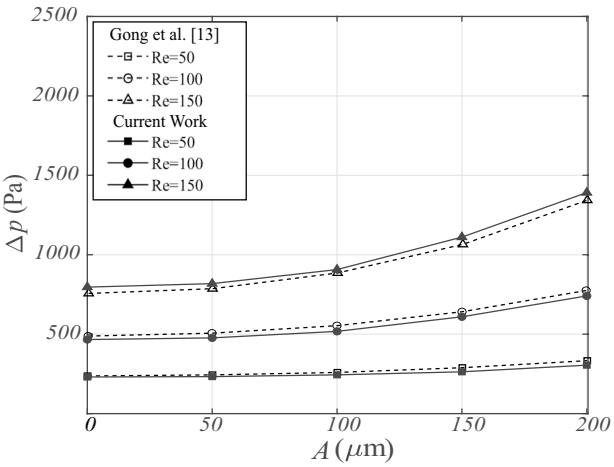

(a) Serpentine microchannel.

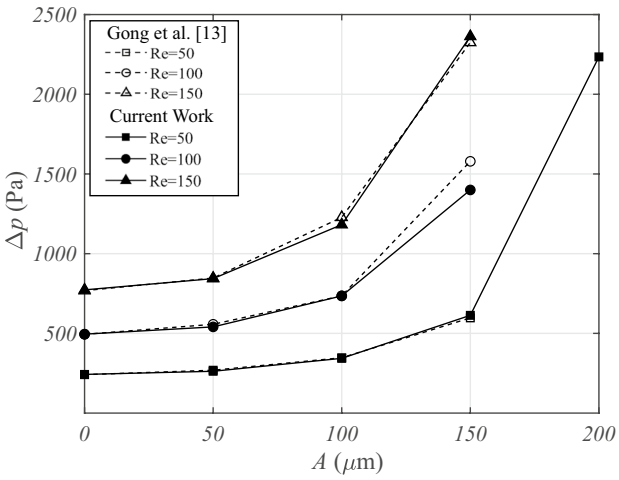

(b) Divergent-convergent microchannel.

Fig. 4 Comparison of present results for Δp vs. A, for $Re = \{50, 100, 150\}$, to results of Gong et al. [13]

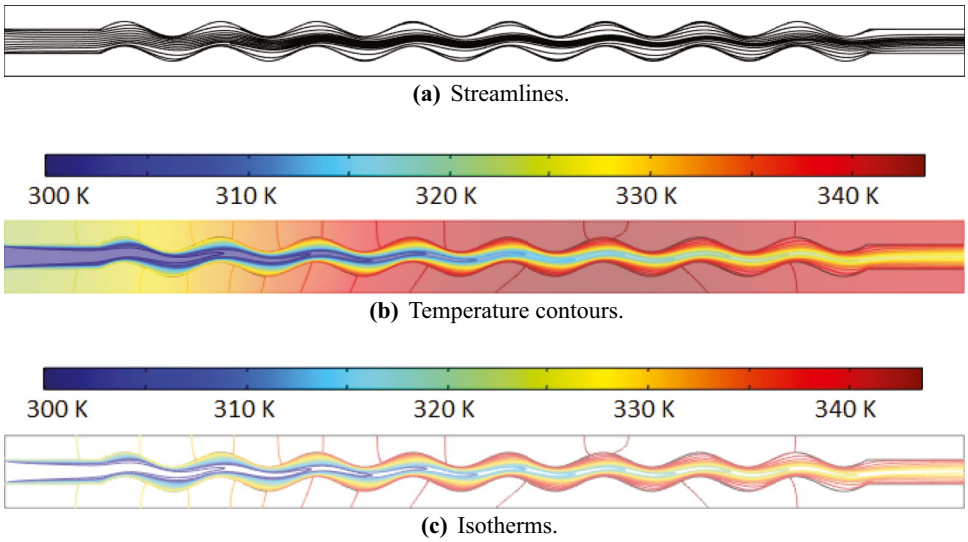

(a) Streamlines.

(b) Temperature contours.

(c) Isotherms.

Fig. 5 Streamlines, temperature contours and isotherms for a serpentine microchannel for $A = 150\ \mu$m and $Re = 100$

[13], but quantitatively they are also very close; the maximum absolute value of the percentage difference is found to be less than 5%. Importantly, for the diverging-converging channel, a complete comparison is not possible since Gong et al. [13] did not include results for wave amplitude of 200 μm. For this amplitude, our results show that, regardless of the value of Re number, the values of Δp are exceedingly high due to the narrow sections in this layout. Thus, in Fig. 4b we have included only Δp for $Re = 50$, with those for $Re = 100$ and 150 being 5.7 kPa and 11.2 kPa, respectively. On the other hand, Figs. 5 and 6 illustrate – qualitatively – the numerical results with wave amplitude $A = 150\ \mu$m, and $Re = 100$, as streamlines, temperature contours and isotherms, respectively, all computed at the mid-plane $z = 0$, for the entire device; i.e., the copper block and the wavy microchannel designs. Though not included here, results for other values of the parameters have shown similar behavior.

The corresponding results for the serpentine design are shown in Figs. 5a, b, c. From Fig. 5a, the evolution of the flow patterns along the microchannel can be clearly seen as the uniform flow at the inlet and develops into periodic patterns in which the streamlines are closer to each other in regions near the channel centerline, revealing larger local velocities, while developing again into a new-uniform flow near its outlet. Influence of the hydrodynamics on the heat transfer is shown in Figs. 5b, c, where it is clear that the temperature field at the entrance is uniform and develops as the fluid travels along the channel, advecting the energy supplied toward the outlet. Importantly, however, is that (a) both isotherms and temperature contours do not have periodic patterns, and (b) larger temperature changes occur upstream of and at the crests of the wavy surfaces, especially at the bottom surface in the central section of the channel where the heat flux is supplied. Another feature from Figs. 5b, c is that temperature

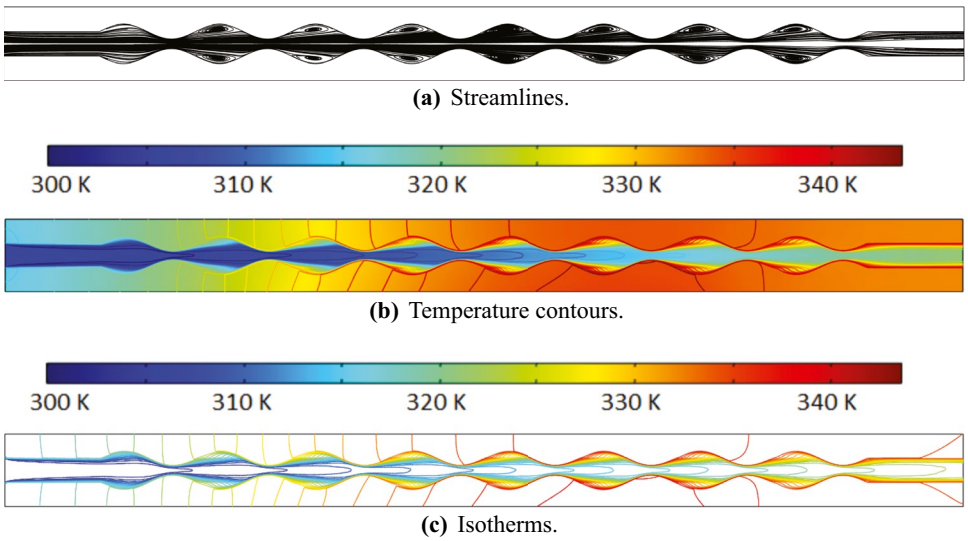

(a) Streamlines.

(b) Temperature contours.

(c) Isotherms.

Fig. 6 Streamlines, temperature contours and isotherms for a convergent-divergent microchannel for $A = 150\ \mu$m and $Re = 100$

contours in the copper domain are homogeneous, spanwise, due to very high thermal conductivity of the block, but they increase along the streamwise direction from a value close to that of the fluid at the inlet, to a maximum in the region where the heat influx occurs, with a subsequent decrease towards the fluid outlet, due to the advective process from the cooling water. For the divergent-convergent channel array, the results are shown in Figs. 6a, b, c. In general similar overall hydrodynamic and thermal characteristics can be observed in this design as compared to the previous system. However, from the figures some differences in the details can be observed. For instance, although periodic patterns also occur in this layout, Fig. 6a illustrates that the uniform flow at the inlet develops into a streamlined flow in the narrow middle section with recirculation zones appearing at the crests of the wavy configuration, thus creating larger pressure drops (as confirmed in Fig. 4b). It is to be noted that these secondary flows are only present in channels with large A but absent for those with low wave amplitude (e.g., $A = 0$ or $A = 50\ \mu$ m). Such a significant increase in pressure drop caused by the narrow section in the divergent-convergent channel may hamper the positive effect in increasing heat transfer, thus reducing the effectiveness of the entire device. As expected, the flow field directly affects the transfer of energy, shown in Figs. 6b, c, as both the isotherms and temperature contours reflect the advective effect from the flow with higher values occurring at the channel surfaces, but with overall aperiodic streamwise patterns. Again, similarly to the case of the serpentine microchannel, the temperature contours in the copper block for the divergent-convergent array are spanwise homogeneous due to its high thermal conductivity. Again, it is observed that the solid temperature increases along the x-direction due to the advective process from the cooling water. At the inlet its value is close to that of the entering fluid, to a maximum in the region where the heat influx occurs, and a subsequent decrease towards the fluid outlet.

4.2 Averaged energy balance equations

We now focus on the averaged energy-balance equations used to quantitatively characterize the performance of the microchannel in lieu of the Nusselt number. As pointed out earlier, Nusselt numbers are effective in providing generality to the analysis of heat transfer in thermal energy systems. However, this generality may come at a cost of accuracy in the results since uncertainties arising due to assumptions embedded in its definition, including the existence of a heat transfer coefficient or that of a unique/identifiable characteristic temperature difference which, for simple devices it may be possible, for systems with high level of complexity it is extremely difficult to deal with [20–26]. Thus, if accuracy is the goal, it is better to compute the heat rate directly. Here, our rationale stems from the methodology laid out by Motamedi et al. [24] and Cobian-Iñiguez et al. [25] to analyze heat exchangers with constant wall temperatures. However, the current work addresses a thermal device receiving a constant heat rate; i.e., $Q_{in} = q'' A_{base} = 7.05$ J, where A_{base} is the projected area at which the heat flux boundary condition is applied (on the bottom surface). The flow speeds are presented with respect to their corresponding Reynolds numbers Re. The range in Reynolds number is $Re \in [50, 150]$, with specific values $Re = \{50, 100, 150\}$. By taking a fixed streamwise location, x, along the microchannel as a reference point, the corresponding cross-sectional-averaged values of pressure $\overline{p}$, streamwise flow velocity $\overline{u}$, and the fluid temperature $\overline{T}$, all derived from local values – obtained from solutions of the governing Eqs. (2)-(6) – are given as

$$\overline{p} = \frac{1}{A}\int_A p\, dA; \qquad \overline{u} = \frac{1}{A}\int_A (\mathbf{u}\cdot\mathbf{n})\, dA; \qquad \overline{T} = \frac{\int_A (\mathbf{u}T\cdot\mathbf{n})\, dA}{\int_A (\mathbf{u}\cdot\mathbf{n})\, dA}. \tag{8}$$

In Eq. (8), A is the cross-sectional area normal to the unit vector $\mathbf{n}$, associated with the surface of interest $dA = dy\, dz$, at any point in the streamwise direction x; p, $\mathbf{u}$ and T, are the local values of fluid pressure, its velocity vector and the corresponding fluid temperature.

By partitioning the wavy-section of the channel into a N-number of subsections (in this work, $N = 8$) of constant length ΔL, an associated control volume – illustrated in Fig. 7 – can be first defined, and then used, to compute the inlet- and outlet-average values of fluid velocity and temperature. Thus, based on this control volume, an energy balance provides the net heat rate Q advected by the fluid, in the selected subsection, as

$$Q_y^B + Q_y^T + 2Q_z + \rho_f \overline{u} A c_{p,f} \overline{T}(x_i^*) - \rho_f \overline{u} A c_{p,f} \overline{T}(x_{i-1}^*) = 0, \tag{9}$$

where $Q_y^B = q''^B{}_y A_{p_{xz}}$, $Q_y^T = q''^T{}_y A_{p_{xz}}$, and $Q_z = q''{}_z A_{p_{xy}}$, with $\sum Q = Q_y^B + Q_y^T + 2Q_z$ (cf. Fig. 7), are – respectively – the corresponding heat transfer rates by diffusion from the copper block into the fluid in the channel. The net heat rate Q_j advected by the fluid in the selected subsection j, which is equal to the heat input to the fluid by conduction from the block to the side walls of the channel, is given as

$$Q_j = \rho_f \overline{u} A c_{p,f} \left[\overline{T}(x_j^*) - \overline{T}(x_{j-1}^*)\right], \tag{10}$$

where $x_{j-1}^* = x^*([j-1]\Delta L)$ and $x_j^* = x^*(j\Delta L)$, for $j = 1, 2, \ldots, N$, represent the location of the cross-section plane of the j–th subsection and Q_j is the corresponding heat rate. The total heat transferred by the device, Q_T, is given by

$$Q_T = \left(\sum_{j=1}^{N=8} Q_j\right) + Q_{L_{x-in}} + Q_{L_{x-out}} = \rho_f \overline{u} A c_{p,f} \left[\overline{T}_{out} - T_{in}\right], \tag{11}$$

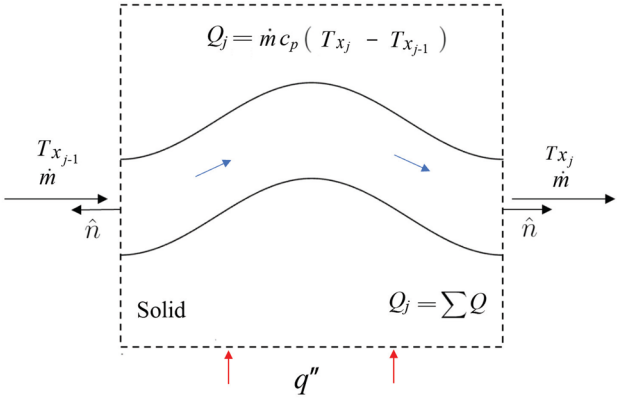

Fig. 7 Control volume of the j-th subsection of the microchannel

where T_{in} is the uniform fluid temperature at the inlet and $\overline{T}_{out}$ is the average fluid temperature at the outlet. Also x^* is the local streamwise coordinate defined before and shown in Fig. 1, and $Q_{L_{x-in}}$ and $Q_{L_{x-out}}$ are, respectively, the heat transfer contributions at the entrance and exit straight-sections.

The corresponding results from the methodology are shown – for the two microchannel layouts – in Fig. 8 as a fraction of the inlet heat rate in the entire device Q/Q_{in}, transferred (advected by the fluid) at each section of the device – and its cumulative values – for a sample amplitude of $A = 150\ \mu$m and $Re = \{50, 100, 150\}$, and in Fig. 9 in terms of the spanwise-averaged fluid temperature distribution $\overline{T}(x)$, in the microchannel, for $A = \{0, 50, 100, 150, 200\}\ \mu$m, and the same values of the Re number. From Fig. 8, with Fig. 8a for the serpentine array and Fig. 8b for the divergent-convergent geometry, it can be observed that, as expected, the fraction of the heat rate advected by the fluid at each section is not constant, but varies both along the streamwise direction, and with Re number. However, it is to note that, for all cases considered (i.e., devices analyzed), the largest values occur at the inlet section (with contributions of about 20% for the serpentine channel and 30% for the divergent-convergent device) and those in the middle (sections 2-6) with contributions of about 10-15% in both cases, with the smallest values appearing downstream of the corresponding channel; i.e., at the last three sections of the device (with contributions of less than 8.5% and 6%, respectively, for the serpentine- and divergent-convergent configurations), even though the heat influx, Q_{in}, is applied in the region comprised by sections 2-7. Furthermore, for both designs, the Q/Q_{in} distribution (from largest values taking place at the inlet section to the smallest at the outlet), changes as Re number increases, with a smooth decline in Q/Q_{in} for $Re = 50$, to a decrease-increase-decrease transition for $Re = 100$ and, more pronounced, for $Re = 150$. This difference is also reflected in the distribution of the cumulative values of Q/Q_{in} for the three Re numbers considered (as

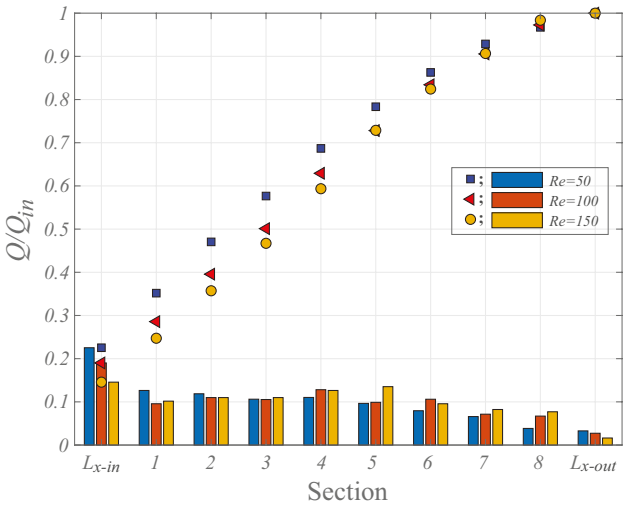

(a) Serpentine microchannel.

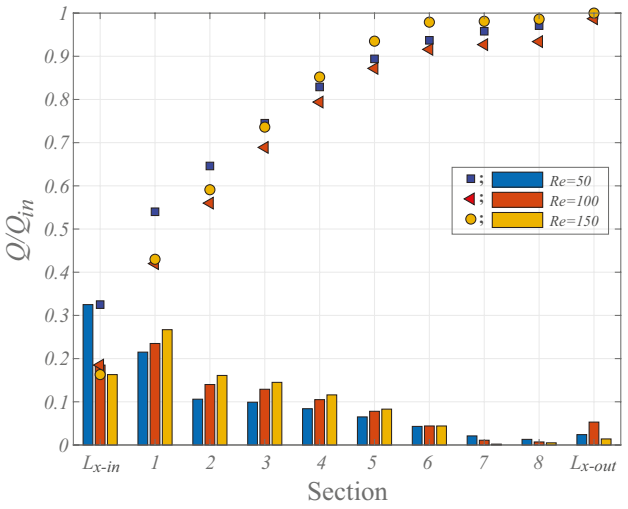

(b) Divergent-convergent microchannel.

Fig. 8 Fraction of inlet heat rate, Q/Q_{in}, transferred at each section of the microchannel for $A = 150\ \mu$m and $Re = \{50, 100, 150\}$

shown in Fig. 8), as they approach the value of unity at the outlet section of the channel, and thought to be due to the capability of the fluid to advect more energy as Re increases. Finally, when comparing the cumulative heat rate for the two types of microchannel layouts, from Figs. 8a, b, it is clear that the amount of energy exchanged at each section is different for each design; for instance, 90% of the possible heat input exchanged is achieved at section 7 by the serpentine array and section 6 by the divergent-convergent layout, indicating that the latter may be more effective in the heat transfer enhancement process (though Δp for this type of array can be as high as 10-times that of the serpentine array). It is to be noted that this approach could be supplemented by using the commonly used performance factor (or performance evaluation criterion), to compute the overall effectiveness

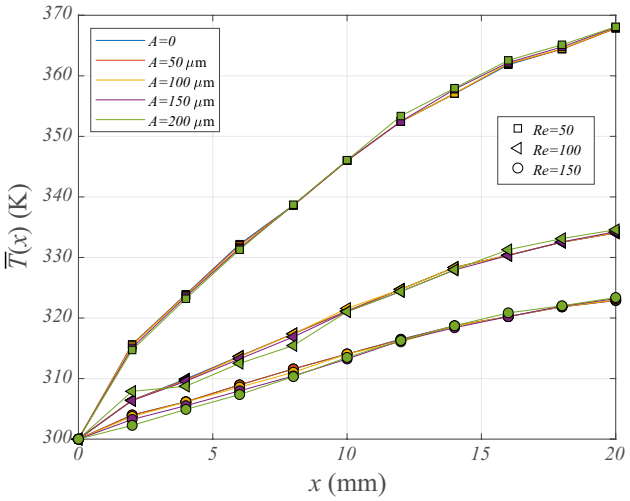

(a) Serpentine microchannel.

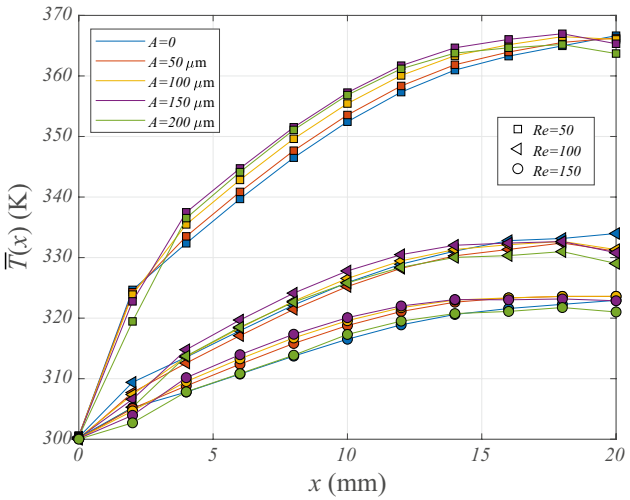

(b) Divergent-convergent microchannel.

Fig. 9 Spanwise-averaged temperature distribution, $\overline{T}(x)$, in the microchannel

of the entire device, However, analysis of its definition and its corresponding application, is beyond the scope of the present investigation.

The aforementioned heat transfer process in the device is corroborated (also illustrated) in Fig. 9a for the serpentine array and Fig. 9b for the divergent-convergent geometry – as two important features of the spanwise-averaged fluid temperature can be identified. Firstly, for a fixed value of *Re*, and for all the amplitudes considered, the temperature difference between inlet and outlet at each section, $\Delta\overline{T}$, reflect the trend in the fraction of the heat rate previously discussed, with larger values in sections closer to the inlet (upstream), and the smaller ones being closer to the channel outlet. Secondly, although the trends are similar, as expected, for a fixed streamwise location x, and a fixed amplitude A, smaller values of $\overline{T}$ take place for larger values of *Re*. This is particularly important since a fluid leaving at a lower temperature has the potential to advect more energy, thus positively affecting the temperature of the block. In this respect, Figs. 9a, b illustrate that, regardless of the difference in values in the middle sections, for the two arrangements the values of $\overline{T}$ for the fluid at the outlet are very close to each other. Finally, Fig. 9 also shows that, surprisingly, as the wave amplitude of the microchannel increases from 0 to 200 μm, the values of $\overline{T}$ do not change significantly. This outcome is thought to be due to the averaging process of the local fluid-temperature field, since our results for the fluid and block temperatures (not shown here), concur with those of Moon et al. [19] indicating that, for a fixed value of *Re* number, as *A* increases the device becomes more effective in transferring the energy out of the system; i.e., the values of the block temperatures decrease proportionally while those of the water continue to increase, indicating larger advection of heat.

5 Concluding remarks

Continuous development of miniature high power-density electronic devices requires cooling systems with better heat removal capabilities and, in this context, single-phase fluid-flow microchannels with wavy geometries offer an avenue to improve the thermal management. For this reason, the general research direction has been on analyzing designs that are able to enhance the transfer of energy, either varying the parameters, the topology or their materials with promising results using the Nusselt number to calculate the heat rate. Although Nusselt numbers are very effective in providing generality to the thermal analysis, they also generate significant uncertainties associated to assumptions embedded in their definition. Therefore, for accuracy purposes it may be better to compute the heat rate directly, without using an intermediate quantities like heat transfer coefficients.

In this work we have considered the analysis of the hydrodynamic and heat transfer characteristics of single-wave wavy microchannels by introducing a methodology of analysis based on local and global energy balances – instead of the common Nusselt number – from three-dimensional velocity and temperature fields, to design more efficient devices. The approach is useful in providing accurate and clear information, at the expense of some generality, to better understand the conjugate heat transfer processes in these devices. Using the procedure, along with the concept of fraction of the total heat rate input onto the specific device, the numerical data for two configurations – namely, serpentine and divergent-convergent layouts – commonly used in electronic cooling applications, have shown that, it is possible to obtain a distribution of both the average fluid temperature along the device, and the corresponding fraction of the inlet heat transfer rate at specific sections to assess their relative performance. The corresponding results demonstrate that, regardless of the values of

wave amplitude, the Reynolds number *Re* (i.e., fluid velocity), plays an important role in the heat transfer enhancement of the corresponding device and in both the fluid and solid block temperatures that are achieved. In addition, as wave amplitude increases, so does the effectiveness of the device in enhancing energy transfer, but at the expense of larger pressure drops. On this point, from the results it is clear that since the two sample designs achieve the objective of dissipating the heat influx to the device, with similar outlet temperature values, their overall effectiveness rely upon the pressure drop necessary to drive the flow, which is lower for the serpentine geometry than that for the diverging-converging microchannel.

Acknowledgements Roxana Durantes acknowledges partial support by the ME Department by a GSA program. Justin Moon was the recipient of a CREST-CEaS fellowship for which we are grateful. This work has been supported by the National Science Foundation under Awards No. HRD-1547723 and HRD-2112554.

Data Availability The datasets generated during and/or analyzed during the current study are available from the corresponding author on reasonable request.

Declarations

Conflicts of interest On behalf of all authors, the corresponding author states that there is no conflict of interest.

References

1. Tuckerman D, Pease R (1981) High-performance heat sinking for VLSI. Electron Device Letters, IEEE 2(5):126–129
2. Kandlikar S, Grande W (2003) Evolution of microchannel flow passages-thermohydraulic performance and fabrication technology. Heat Transfer Engineering 24(1):1–17
3. Tullius J, Vajtai R, Bayazitoglu Y (2011) A review of cooling in microchannels. Heat Transfer Engineering 32(7–8):527–541, paper No.PII 930703154
4. Kandlikar S, Colin S, Peles Y, Garimella S, Pease R, Brandner J, Tuckerman D (2013) Heat transfer in microchannels-2012 status and research needs. ASME J Heat Transfer 135(9), paper No. 091001
5. Mathew J, Krishnan S (2022) A review on transient thermal management of electronic devices. Journal of Electronic Packaging, Transactions of the ASME 144, article No. 010801
6. Lee P, Garimella S, Liu D (2005) Investigation of heat transfer in rectangular microchannels. Int J Heat Mass Transfer 48:1688–1704
7. Xie X, Liu Z, He Y, Tao W (2009) Numerical study of laminar heat transfer and pressure drop characteristics in a water-cooled minichannel heat sink. Appl Therm Eng 29:64–74
8. Harms T, Kazmierczak M, Gerner F (1999) Developing convective heat transfer in deep rectangular microchannels. Int J Heat and Fluid Flow 20:149–157
9. Qu W, Mudawar I (2002) Experimental and numerical study of pressure drop and heat transfer in a single-phase microchannel heat sink. Int J Heat Mass Transfer 45:2549–2565
10. Sasaki S, Kishimoto T (1986) Optimal structure for microgrooved cooling fin for high-power LSI devices. Electronic Letters 22:1332–1334
11. Sui Y, Teo C, Lee P, Chew Y, Shu C (2010) Fluid flow and heat transfer in wavy microchannels. Int J Heat Mass Transfer 53:2760–2772
12. Sui Y, Lee P, Teo C (2011) An experimental study of flow friction and heat transfer in wavy microchannels with rectangular cross section. Int J Thermal Sciences 50:2473–2482
13. Gong L, Kota K, Tao W, Joshi Y (2011) Parametric numerical study of flow and heat transfer in microchannels with wavy walls. ASME J Heat Transfer 133(5), paper No. 051702
14. Vafai K, Zhu L (1999) Analysis of two-layered micro-channel heat sink concept in electronic cooling. Int J Heat Mass Transfer 42:2287–2297
15. Xie G, Chen Z, Sunden B, Zhang W (2013) Numerical predictions of the flow and thermal performance of water-cooled single-layer and double-layer wavy microchannel heat sinks. Numer Heat Transfer, Part A 63:201–225
16. Xie G, Liu J, Liu Y, Sunden B, Zhang W (2013b) Comparative study of thermal performance of longitudinal and transversal-wavy microchannel heat sinks for electronic cooling. ASME J Electronic Packaging 135(2), paper No. 021008
17. Moon J, Pacheco J, Pacheco-Vega A (2018) Heat transfer enhancement in wavy micro-channels through multiharmonic surfaces. In: Proceedings of the ASME 2018 International Mechanical Engineering Congress and Exposition, Pittsburgh, PA, USA, IMECE2018-86425
18. Dash B, Nanda J, Rout S (2022) The role of microchannel geometry selection on heat transfer enhancement in heat sinks: A review. Heat Transfer 51:1406–1424
19. Moon J, Pacheco J, Pacheco-Vega A (2019) Heat transfer enhancement in wavy micro-channels: Effect of block material. In: Proceedings of the 4th World Congress on Momentum, Heat and Mass Transfer (MHMT'19), Rome, Italy, ENFHT-120
20. Pacheco-Vega A, Diaz G, Sen M, Yang K, McClain R (2001) Heat rate predictions in humid air-water heat exchangers using correlations and neural networks. ASME J Heat Transfer 123(2):348–354
21. Pacheco-Vega A, Sen M, Yang K (2003) Simultaneous determination of in- and over-tube heat transfer correlations in heat exchangers by global regression. Int J Heat Mass Transfer 46(6):1029–1040
22. Pacheco-Vega A, Sen M, Yang K, McClain RL (1998) Genetic-algorithm-based-predictions of fin-tube heat exchanger performance. In: Lee J (ed) Proceedings of the Eleventh International Heat Transfer Conference, Taylor & Francis, New York, NY, vol **6**, pp 137–142
23. Pacheco-Vega A (2011) Soft computing applications in thermal energy systems. In: Gopalakrishnan K, Khaitan S, Kalogirou S (eds) Soft Computing in Green and Renewable Energy Systems, vol 269. Springer-Verlag, pp 1–35
24. Motamedi A, Pacheco-Vega A, Pacheco J, Rodic T (2012) Numerical analysis of a multi-row multi-column compact heat exchanger. Journal of Physics: Conference Series 395:1–9, paper No. 012121
25. Cobian-Iniguez J, Wu A, Dugast F, Pacheco-Vega A (2015) Numerically-based parametric analysis of plain fin and tube compact heat exchangers. Applied Thermal Engineering 86:1–13
26. Pacheco-Vega A, Diaz G, Sen M, Yang K (2017) Applications of artificial neural networks and genetic methods in thermal engineering. In: Chhabra R (ed) CRC Handbook of Thermal Engineering, 2nd edn, CRC Press, chap 4.27, pp 1217–1269
27. Chiu W, Jaluria Y, Glumac N (2000) Numerical simulation of chemical vapor decomposition processes under variable and constant property approximations. Numer Heat Transfer, Part A 37(2):113–132
28. Xie G, Wang Q, Sunden B (2009) Parametric study and multiple correlations on air-side heat transfer and friction characteristics on fin-and-tube heat exchangers with large number of large-diameter tube rows. Int J Heat Mass Transfer 29:1–16
29. Arnold D, Brezzi F, Cockburn B, Marini L (2002) Unified analysis of discontinuous Galerkin methods for elliptic problems. SIAM J of Numerical Analysis 39:1749–1779